



This is a repository copy of *Pb, Bi, and rare earth free X6R barium titanate–sodium niobate ceramics for high voltage capacitor applications.*

White Rose Research Online URL for this paper:

<https://eprints.whiterose.ac.uk/198318/>

Version: Published Version

Article:

Fan, Y. orcid.org/0000-0001-9769-5619, Wang, X., Li, H. et al. (5 more authors) (2023) Pb, Bi, and rare earth free X6R barium titanate–sodium niobate ceramics for high voltage capacitor applications. *Applied Physics Letters*, 122. 143901. ISSN 0003-6951

<https://doi.org/10.1063/5.0142200>

Reuse

This article is distributed under the terms of the Creative Commons Attribution (CC BY) licence. This licence allows you to distribute, remix, tweak, and build upon the work, even commercially, as long as you credit the authors for the original work. More information and the full terms of the licence here:

<https://creativecommons.org/licenses/>

Takedown

If you consider content in White Rose Research Online to be in breach of UK law, please notify us by emailing eprints@whiterose.ac.uk including the URL of the record and the reason for the withdrawal request.



eprints@whiterose.ac.uk
<https://eprints.whiterose.ac.uk/>

RESEARCH ARTICLE | APRIL 03 2023

Pb, Bi, and rare earth free X6R barium titanate–sodium niobate ceramics for high voltage capacitor applications

Special Collection: [Energy Conversion and Storage in Functional Dielectrics](#)

Yongbo Fan; Xinzhen Wang; Hongtian Li; ... et. al



Appl. Phys. Lett. 122, 143901 (2023)

<https://doi.org/10.1063/5.0142200>



View Online



Export Citation

CrossMark

Articles You May Be Interested In

Effect of phase transition on the optoelectronic properties of $Zn_{1-x}Mg_xS$

Journal of Applied Physics (October 2012)

Structure, band gap, and Mn-related mid-gap states in epitaxial single crystal $(Zn_{1-x}Mg_x)_{1-y}Mn_yO$ thin films

Journal of Applied Physics (May 2013)

Mg-doped $TlBa_2(Ca_{2-x}Mg_x)(Cu_{2.2}Ti_{0.8})O_{10-\delta}$ ($x = 0, 0.05, 0.15, 0.25, 0.35$) superconductors

Journal of Applied Physics (May 2013)

Time to get excited.
Lock-in Amplifiers – from DC to 8.5 GHz

[Find out more](#)

Pb, Bi, and rare earth free X6R barium titanate–sodium niobate ceramics for high voltage capacitor applications

Cite as: Appl. Phys. Lett. **122**, 143901 (2023); doi: [10.1063/5.0142200](https://doi.org/10.1063/5.0142200)

Submitted: 12 January 2023 · Accepted: 21 March 2023 ·

Published Online: 3 April 2023



View Online



Export Citation



CrossMark

Yongbo Fan,¹  Xinzhen Wang,^{1,2} Hongtian Li,^{3,4} Antonio Feteira,⁵  Dawei Wang,^{4,6}  Ge Wang,^{1,7} Derek C. Sinclair,¹  and Ian M. Reaney^{1,a)} 

AFFILIATIONS

¹Department of Materials Science and Engineering, The University of Sheffield, Sheffield S1 3JD, United Kingdom

²School of Materials Science and Engineering, Shandong University of Science and Technology, Qingdao 266590, China

³Key Laboratory of Nonferrous Materials and New Processing Technology, Ministry of Education, School of Materials Science and Engineering, Guilin University of Technology, Guilin 541004, China

⁴Shenzhen Institute of Advanced Electronic Materials, Shenzhen Institute of Advanced Technology, Chinese Academy of Sciences, Shenzhen 518055, China

⁵Materials and Engineering Research Institute, Sheffield Hallam University, Sheffield S1 1WB, United Kingdom

⁶Functional Materials and Acousto-Optic Instruments Institute, School of Instrumentation Science and Engineering, Harbin Institute of Technology, Harbin 150080, China

⁷Department of Materials, University of Manchester, Manchester M13 9PL, United Kingdom

Note: This paper is part of the APL Special Collection on Energy Conversion and Storage in Functional Dielectrics.

^{a)}Author to whom correspondence should be addressed: i.m.reaney@sheffield.ac.uk

ABSTRACT

0.9Ba(Ti_{1-x}Mg_x)O_{3-x}-0.1NaNbO₃ (BTNN-100xMg) solid solutions are investigated with a view to developing Bi, Pb, and rare earth free, high voltage multilayer ceramic capacitors. Mg doping on the B-site significantly reduced the electronic conductivity and resulted in ceramics that could withstand a pulsed unipolar field of >300 kV/cm (E_{\max}) to give a recoverable energy density of 3.4 J/cm³ at 82.6% efficiency for $x = 0.01$. The high E_{\max} is accompanied by a high dielectric permittivity ($\epsilon' \sim 1700$ at room temperature) with temperature-stable dielectric permittivity of $\Delta\epsilon/\epsilon_{298K} \leq \pm 15\%$ and loss tangent $\tan \delta < 0.02$ from 116 to 378 K, corresponding to an X6R designation in the Electronic Industry Alliance codes.

© 2023 Author(s). All article content, except where otherwise noted, is licensed under a Creative Commons Attribution (CC BY) license (<http://creativecommons.org/licenses/by/4.0/>). <https://doi.org/10.1063/5.0142200>

As the market for electric and hybrid vehicles expands, the demand for multilayer ceramic capacitors (MLCCs) that operate as energy storage devices is increasing. Ceramics are generally more stable than polymers at high temperature (>100 °C), making MLCCs especially suited for near engine applications as they do not require heat management systems.¹ Recently, research has focused on improving the energy storage performance of electroceramics for MLCCs to replace tantalum electrolytic and metalized film capacitors with a rated voltage at >400 V.² The relative permittivity (ϵ_r) of BaTiO₃ dielectric layers decreases sharply at high DC bias, and therefore, it is difficult using current commercial compositions to develop MLCCs with both a high capacitance and volumetric efficiency at high operating fields.^{3,4}

Dielectric materials for MLCCs in consumer electronics that are utilized at low fields are adequately characterized by the dielectric permittivity (ϵ'), loss tangent ($\tan \delta$), and dielectric temperature stability ($\Delta\epsilon/\epsilon_{298K}$) since they provide a direct and accurate representation of the dielectric performance close to their operating conditions. However, to develop ceramics suitable for high-field applications, their performance at >100 kV/cm needs to be evaluated. Such measurements are difficult to obtain using classic LCR/impedance analyzers, and characterization using polarization–electric field (P–E) measurements is preferred. The key parameters for the evaluation of the high field performance of a dielectric material are recoverable energy storage density (W_{rec}) and efficiency (η), which may be extracted from the following P–E loop

$$W_{\text{rec}} = \int_{P_r}^{P_{\text{max}}} E \, dP, \quad (1)$$

$$\eta = \frac{W_{\text{rec}}}{W_{\text{total}}} * 100\%, \quad (2)$$

where P_{max} , P_r , and W_{total} are the maximum polarization, remnant polarization, and total energy density, respectively. Although the definition of W_{rec} and η are from energy storage rather than dielectric perspective, they may be converted following the relation:

$$P = \epsilon E. \quad (3)$$

As a result, W_{rec} and η correlate with dielectric permittivity (ϵ') and $\tan \delta$, respectively, at a given electric field. Although the connection between ferroelectric and dielectric performance of a material is straightforward from the above equations, attention is required when evaluating dielectric properties from a quasi-static P-E measurement. The electrical response of a dielectric material is heavily dependent on the starting state, magnitude, frequency, and shape of the testing signal.^{5–8} Testing should be done as close to the condition of interest as possible. Despite such limitations, ferroelectric measurements have been widely adopted to develop high voltage MLCCs. Analogous to strain–electric field (S-E) measurements,⁹ W_{rec} and η provide an extremely convenient way to visualize the performance of a dielectric by considering the area depicted by the P-E loop, which enables the wider scientific community to engage in the development of capacitor materials. For example, a wide range of polymers are now being adopted for low temperature applications and may be directly compared with electroceramics using P-E loops.¹⁰ It is evident that W_{rec} and η are more convenient and suitable than evaluating ϵ' and $\tan \delta$ at high field and are an effective method to test and optimize energy storage and high voltage performance.

Based on Eq. (1), approaches to achieve a high W_{rec} , in, e.g., perovskites, include the following: (i) enhancing the dielectric breakdown strength (BDS) by optimizing the microstructure (eliminating pores, and controlling grain growth),¹¹ establishing a homogeneous electrical microstructure^{12–14} through control of defect chemistry, and choosing materials with a large intrinsic bandgap such as NaNbO_3 ;¹⁵ (ii) increasing polarisability per unit cell volume by incorporating d_0 (Ti^{4+} and Nb^{5+}) and electron lone-pair ions (Bi^{3+} and Pb^{2+}) on the B- and A-sites, respectively;^{16,17} and (iii) enhancing $P_{\text{max}}-P_r$ by inducing relaxor behavior through alloying or doping to make pseudo-ternary and quaternary solid solutions.¹⁸ Based on Eq. (2), a higher η is achieved by either inducing relaxor behavior (narrower P-E hysteresis loop) or reducing the field difference between antiferroelectric and ferroelectric states in antiferroelectric compositions.^{19,20}

To design the composition presented in this study, both previous research and several practical considerations were taken into account, i.e., the avoidance of rare earth (RE) ions, Bi, and Pb. Previous research on high energy density ceramic capacitors has primarily focused on systems based on BaTiO_3 (BT), BiFeO_3 (BF), $\text{K}_{0.5}\text{Na}_{0.5}\text{NbO}_3$ (KNN), $\text{Na}_{0.5}\text{Bi}_{0.5}\text{TiO}_3$ (NBT), NaNbO_3 (NN), AgNbO_3 (AN), and lead-containing materials.^{21–27} Among them, BT is currently most widely used as a base material for class II MLCCs and was thus selected for this study. NN, which has the highest bandgap among the common lead-free perovskites,¹⁵ was chosen as part of the solid solution to potentially enhance breakdown strength and improve E_{max} . Mg^{2+} was used as a dopant on the B-site to tune conductivity (p vs n) and

achieve a higher reliability for the dielectric.^{28,29} Bi^{3+} was not adopted as a dopant or alloying addition due to its thermodynamic incompatibility with Ni electrodes, which would necessitate the use of expensive Pt or Ag/Pd internal electrodes for MLCCs, making them less attractive from a practical perspective.^{21,30,31} Pb^{2+} was excluded due to its negative health effects,³² and RE ions are not considered due to their cost, scarcity, and geopolitical uncertainty of their availability.³

The piezoelectric, dielectric, and ferroelectric properties of BT-NN solid solutions have been reported previously,^{33–35} but to date its potential as a high voltage, temperature stable dielectric has not been considered due to its high conductivity. Here, we report the crystal structure, electrical microstructure, and dielectric and energy storage performance of BTNN-100xMg ceramics. Their potential for use in high voltage capacitors is discussed and the next steps toward commercialization assessed. BTNN-100xMg ($x = 0, 0.005, 0.01, 0.02, 0.05$) ceramics were prepared by conventional solid state reaction method. The fabrication and characterization methods are detailed in the [supplementary material](#).

The XRD patterns of BTNN-100xMg ceramics are shown in Fig. 1, which exhibit a mixture of perovskite phases, with a secondary $\text{Ba}_5\text{Ti}_{14}\text{Nb}_2\text{O}_{39}$ (PDF 00-038-1431) phase detected for $x < 0.02$, $\text{Ba}_{11}\text{Ti}_{28}\text{O}_{66.5}$ (PDF 01-073-5502) for $x = 0.02$, and $\text{Ba}_4\text{Ti}_{11}\text{O}_{26}$ (PDF 01-083-1459) for $x = 0.05$. The changes in XRD profile of the secondary phase are shown in Fig. S1. The peaks of perovskite phases, as exemplified by (110) in Fig. 1(b), shift to higher angles with $x \leq 0.02$, then back to lower 2θ at $x = 0.05$. Effectively, the unit cell volume initially shrinks and then expands. The appearance of a Nb containing second phase for $x < 0.02$ is consistent with volatilization of Na which leaves Nb in excess, compensated by the formation $\text{Ba}_5\text{Ti}_{14}\text{Nb}_2\text{O}_{39}$ second phase. As Mg concentration increases, however, the second phase for $x \geq 0.02$ no longer contains Nb suggesting that it is retained within the perovskite matrix. The simplest explanation is that Mg enters in small concentrations onto the perovskite A-site, compensating in part for Na-ion vacancies and allowing Nb to be retained. However, we note that Mg^{2+} in 12-fold (A-site) coordination is unknown since its ionic radius is normally considered too small to occupy the cuboctahedral volume. Mg^{2+} in small concentrations on the A-site, however, would explain the reduction in unit cell volume for $x \leq 0.02$. The expansion of the lattice for $x > 0.02$ may relate to the

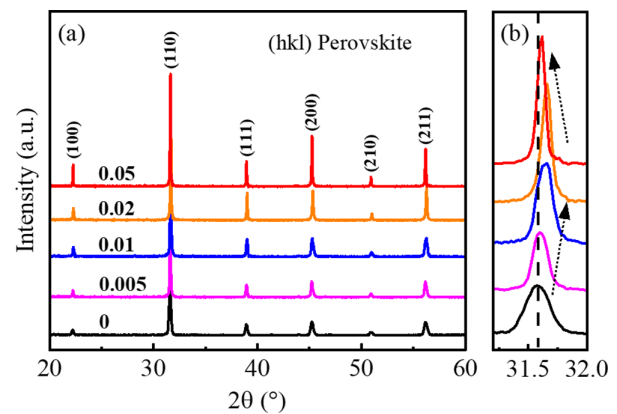


FIG. 1. (a) XRD patterns of BTNN-100xMg ceramics sintered at 1440–1460 °C for 2 h. (b) Expanded (110) peaks in the range of 31° and 32°.

substitution of Mg^{2+} for Ti^{4+} ions onto the B-site, which is compensated by O-vacancies giving rise to a small repulsive force on the B-site sublattice. Mg^{2+} is typically known to occupy the B-site in perovskite titanates.^{36,37} The substitution of Mg onto the B site is consistent with changes to the A_{1g} vibration mode shown at ~ 770 and ~ 830 cm^{-1} in the Raman spectra in Fig. S3.³⁸

Rietveld refinements were performed on the XRD data to analyze the crystal structure of the samples. A single or combination of tetragonal P4mm and cubic $\text{Pm}\bar{3}\text{m}$ space group was adopted in the fitting with the best result obtained with coexistence of the two symmetries as shown in Fig. S2. The refinements confirm that the unit cell volume of these two phases decreases slightly and then increase with x , as shown in Fig. S4. The phase fraction of P4mm and $\text{Pm}\bar{3}\text{m}$ is $\sim 50:50$ for $x \leq 0.02$, but a significant increase in the proportion of cubic phase is observed for $x = 0.05$. This trend is confirmed by the disappearance of the B_1 mode at ~ 301 cm^{-1} in the Raman spectra (Fig. S3).³⁹ Based on the ionic displacements resolved in the Rietveld refinement, the spontaneous polarization of the BTNN-100xMg samples is estimated using the Shimakawa model, with details shown in the [supplementary material](#).^{40,41} As shown in Fig. S2(d), the total spontaneous polarization decreases from ~ 6 to ~ 1 $\mu\text{C}/\text{cm}^2$ with increasing dopant concentration.

The microstructure of BTNN-100xMg ceramics display dramatic changes with x , as shown in Fig. S5. For $x < 0.02$, the average grain size is ~ 0.5 μm , with some extremely small grains and a few that are larger but with none > 2 μm . For $x = 0.02$, the grain boundaries become distinct accompanied by an increase in the average grain size to ~ 1.5 μm . For $x = 0.05$, the average grain size increases dramatically to > 10 μm . The increase in grain size is commensurate with the onset of acceptor Mg^{2+} doping onto the B-site which has been shown in BT based materials to enhance mass transfer.⁴²

The permittivity temperature plots of BTNN-100xMg ceramics are shown in Fig. 2(a). In the undoped BT10NN sample, the broad phase transition suggests that the transformation from cubic to tetragonal phase is not at a distinct Curie temperature, but rather over > 100 K. This is also the case for $x = 0.005$ and $x = 0.01$ and is attributed to an inhomogeneous composition and microstructure. However, a single, broad, and large peak in permittivity is observed for $x = 0.02$, which decreases in temperature with increasing dopant concentration. The high dielectric loss of $x = 0.05$ suggests that the high permittivity is not entirely due to the contribution of the polar phase but also due to space charge from clusters of defects, most likely O vacancies. As

shown in Fig. S6, the best dielectric temperature stability is achieved in $x = 0.01$, which meets the commercial specification of X6R MLCC ($\Delta C/C_0 \leq \pm 15\%$ from -55 to 105 $^\circ\text{C}$). For $x = 0.01$, an additional dielectric anomaly is detected at around 32 K in Fig. 2(b), which may be associated with a transition to a lower symmetry phase.

The effect of Mg^{2+} dopant on the conduction mechanism of BTNN-100xMg ceramic is shown in Fig. S7. As the Mg^{2+} concentration increases, the conduction shifts from n - to p - then back to n -type for $x = 0.05$. The shift from n to p is due to acceptor doping. A possible mechanism for the shift back to n is the excessive grain growth that limits the level of grain boundaries in the ceramic, which means there is less channels for oxygen to enter the samples during the cooling process from sintering. This would leave more oxygen vacancies for $x = 0.05$, which makes the sample n -type and more conductive. The total resistivity at 550 $^\circ\text{C}$ in air increases, then drops at $x = 0.05$, which may be due to an increase in the concentration of oxygen vacancies with acceptor doping.

To investigate the electrical microstructure of the BTNN-100xMg ceramics, impedance data were collected on samples between 450 and 650 $^\circ\text{C}$. The contribution of different components could be distinguished by analyzing the frequency spectrum of the imaginary part of impedance (Z'') and imaginary part of the modulus (M''), as shown in Figs. 3(a) and 3(b). It is clear from Fig. 3(b) that the M'' peaks of $x \leq 0.01$ are broad, consisting of at least two Debye peaks with very similar peak frequencies, which makes it difficult to identify the contributions from individual electrical components. However, the M'' peaks begin to split at higher dopant levels. Peak frequencies differ by at least two orders of magnitude, providing an opportunity for more detailed analysis. Thus, data from $x = 0.02$ are selected to illustrate how the electrical microstructure of these ceramics may be resolved from their impedance responses. The capacitances of the electrical components of $x = 0.02$ are extracted from the M'' peaks as shown in Fig. 3(c), and their Curie-Weiss behavior is fitted in Fig. 3(d). Details of the analyses are in the [supplementary material](#).

From Fig. 3, we conclude that an electrical core-shell structure is shown in the impedance spectra of BTNN-100xMg ceramics. At low dopant levels, the core and shell regions share a similar capacitance of ~ 35 pF/cm (as corrected for overall sample geometry), and a similar f_{max} at 10 – 100 kHz. For $x > 0.01$, the grains grow significantly, and the resistance of the shell becomes much larger than that of the core, which separates the characteristic frequency, allowing a more detailed analysis of those regions. f_{max} for the core component shifts to much

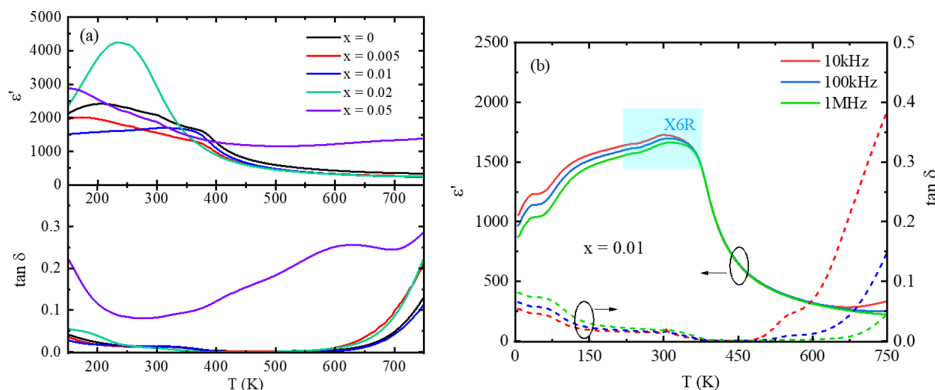


FIG. 2. (a) Temperature dependence of ϵ' and $\tan \delta$ for BTNN-100xMg ceramics at 100 kHz from 150 to 750 K. (b) ϵ' and $\tan \delta$ at different frequencies in the temperature range of 6–750 K for $x = 0.01$, with the X6R specification depicted with the cyan area.

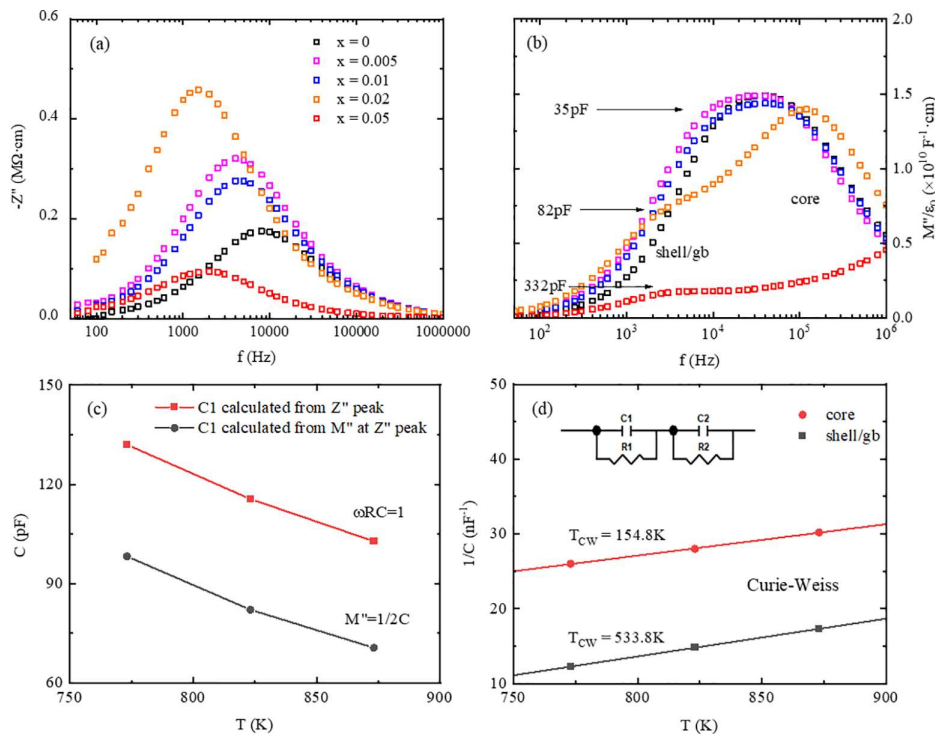


FIG. 3. The frequency dependence of (a) Z'' and (b) M'' of BTNN-100xMg ceramics at 550 °C. (c) The capacitance of shell in the grain of $x = 0.02$ extracted from the Z'' value and M'' value, respectively. (d) The Curie-Weiss fitting of the capacitance of core and shell/gb component, with the equivalent circuit and Curie-Weiss temperature marked in the graph.

higher frequency (off scale) with x increased to 0.05, indicating a significantly more conductive core region in the sample, which could be further investigated.

The conductivity and activation energy of the charge carriers in the ceramic and the core-shell components correspond to the response of R_1 and R_2 in the equivalent circuit, respectively. As indicated in Figs. 4(a) and 4(b), the shell components have, overall, a lower conductivity and higher activation energy than the core components. When comparing Figs. 4(a) and 4(b) with Fig. S8, it is evident that the resistive response of the ceramics is dominated by the shell component. Since no dielectric anomaly was detected in the dielectric temperature spectrum above $\sim 100^\circ\text{C}$, an extrapolation of Arrhenius plot was performed to deduct the conductivity closer to room temperature. As shown in Figs. 4(c) and 4(d), $x = 0.02$ have the most resistive shell component and highest activation energy for both the core and shell components, which potentially improves the breakdown strength under applied field. However, this is not the case with the P-E measurement of the samples. This may due to the grain growth, which increased the volume fraction of the electrically more conductive core region, based on M'' - f spectra.

The spontaneous polarization of BTNN-100xMg ceramics decrease with increasing dopant level, as shown in Fig. S2(d). This trend could also be observed in the P-E loops shown in Fig. 5(a), with polarization measured at 380 kV/cm decreasing from ~ 28 to $\sim 24 \mu\text{C}/\text{cm}^2$ for $x = 0.00$ to 0.02. However, the measured polarization value is significantly larger than the calculated spontaneous polarization ($\sim 5 \mu\text{C}/\text{cm}^2$). The difference in maximum polarization measured in P-E loop and spontaneous polarization is often the case for relaxor materials. A crossover from dielectric to semiconductor behavior is seen for $x > 0.02$.

As shown in Fig. S9, the I-V curve of Au-5Mg-Au device is typical for a double Schottky barrier device.⁴³

In BTNN-100xMg ceramics, the optimum energy storage performance was achieved for $x = 0.01$, which has $W_{\text{rec}} = 3.4 \text{ J}/\text{cm}^3$ with η of 82.6% at 400 kV/cm. As shown in Fig. 5(b), E_{max} and energy storage density of the samples increased, whereas the efficiency of energy storage dropped with increasing dopant concentration. The enhanced energy storage performance may associate with a more resistive core region with elevated activation energy. Additionally, $x = 0.01$ shows a broad plateau in permittivity as a function of temperature. In Figs. 5(c) and 5(d), the energy discharge performance of $x = 0.01$ is evaluated in an underdamped and overdamped R-C circuit. In both scenarios, the sample is able to discharge the electrical energy to the resistor within 1 μs .

In this paper, the criteria for evaluating energy storage dielectric materials are briefly discussed. The crystal structure of BTNN-100xMg ceramics were analyzed through Rietveld refinement of the x-ray data to obtain the phase assemblage and the microscopic spontaneous polarization of the ceramics. The electrical microstructures of the Mg-doped BTNN ceramics were analyzed with impedance spectroscopy data and ϵ_r vs T assessed. With an optimized W_{rec} of $3.4 \text{ J}/\text{cm}^3$, η of 82.6% at 400 kV/cm, and meeting the X6R specification, Mg-doped BTNN ceramics are a good candidate for high voltage MLCCs. However, 1440°C is too high to use Ni internal electrodes in the fabrication of MLCCs and glass additions would be required to reduce the sintering temperature and, thus, potentially make compositions compatible with base metal technology. Preliminary results with 1% glass addition have suggested a reduction in sintering temperature is achievable while retaining a usable dielectric response but further work is required to develop reliable MLCC formulations. Nonetheless, these

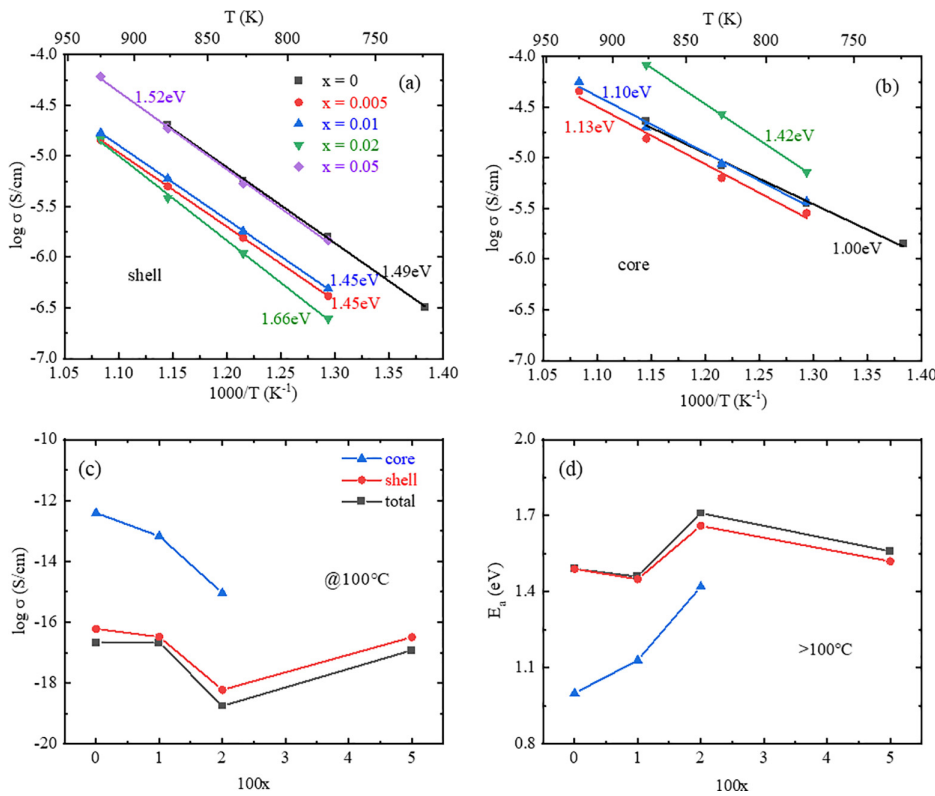


FIG. 4. Arrhenius plot of the (a) shell and (b) core components of the BTNN-100xMg ceramics, with the corresponding activation energy labeled near the fitted line. (c) Extrapolated log conductivity ($\log \sigma$) at 100°C and (d) activation energy $>100^\circ\text{C}$, for the different components for BTNN-100xMg ceramics derived from conductivity Arrhenius plots.

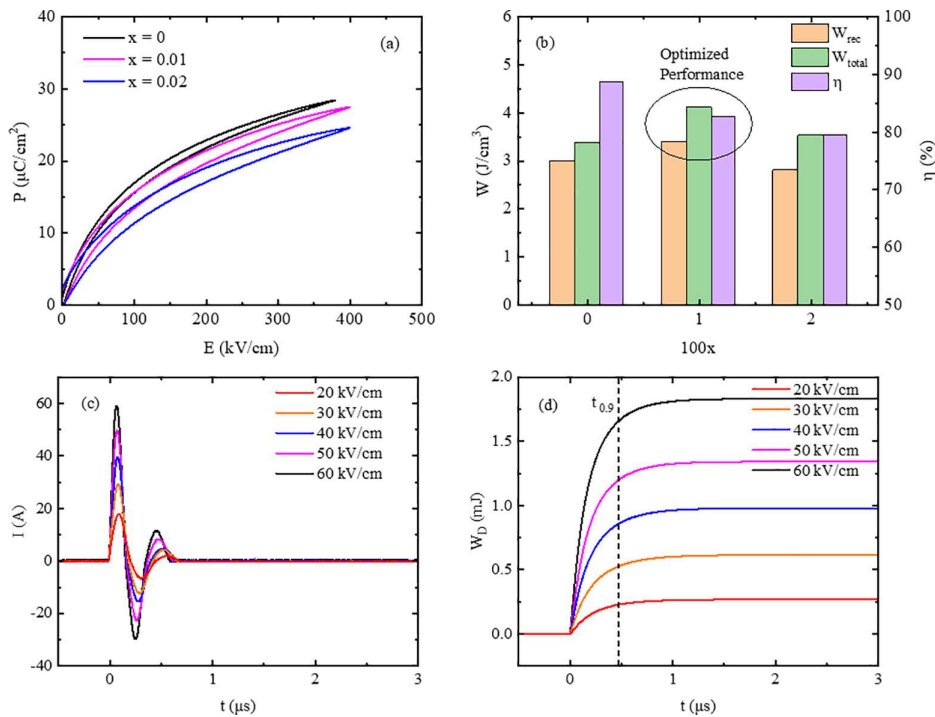


FIG. 5. (a) Polarization vs electric field for BTNN-100xMg ceramics at room temperature. (b) The dependence of energy storage performance (W_{rec} , W_{total} , η) on dopant level. (c) The discharge current of 1 Mg measured in an underdamped R-C circuit and (d) the discharged energy of the same sample in an overdamped R-C circuit, with different charging field.

Downloaded from http://pubs.aip.org/apl/article-pdf/doi/10.1063/5.0142200/16820693/143901_1_5.0142200.pdf

compositions show promise and represent a sensible direction for research into high voltage/energy storage capacitors where there is a clear commercial need for Pb, Bi, and RE free dielectric compositions.

See the [supplementary material](#) for details that include experimental methods, impedance analyses of $x = 0.02$, Rietveld refinement of XRD pattern, the derived contribution of ions to spontaneous polarization, Raman spectra, scanning electron microscopy images, temperature coefficient of capacitance data, atmosphere impedance measurements, Arrhenius plots, summary of energy storage performance, and I–V curve of $x = 0.05$.

Yongbo Fan and Ian M. Reaney would like to acknowledge Innovate UK and Engineering and Physical Science Research Council Grant Nos. TS/W012774/1 and EP/X016463/1, respectively. The authors would like to thank the support of Functional Material and Devices group in the University of Sheffield.

AUTHOR DECLARATIONS

Conflict of Interest

The authors have no conflicts to disclose.

Author Contributions

Yongbo Fan: Conceptualization (equal); Formal analysis (equal); Investigation (equal); Writing – original draft (equal). **Xinzhen Wang:** Investigation (equal); Writing – review & editing (equal). **Hongtian Li:** Investigation (equal). **Antonio Feteira:** Resources (equal). **Dawei Wang:** Resources (equal); Writing – review & editing (equal). **Ge Wang:** Conceptualization (equal); Investigation (equal); Supervision (equal); Writing – review & editing (equal). **Derek Clark Sinclair:** Formal analysis (equal); Supervision (equal); Writing – review & editing (equal). **Ian M. Reaney:** Conceptualization (equal); Funding acquisition (equal); Project administration (equal); Supervision (equal); Writing – review & editing (equal).

DATA AVAILABILITY

The data that support the findings of this study are available from the corresponding author upon reasonable request.

REFERENCES

- Y. H. Song, J. H. Hwang, and Y. H. Han, *Jpn. J. Appl. Phys., Part 1* **44**(3R), 1310 (2005).
- J. Stewart, J. Neely, J. Delhotal, and J. Flicker, “DC link bus design for high frequency, high temperature converters,” *2017 IEEE Applied Power Electronics Conference and Exposition (APEC)* (IEEE, FL, 2017), pp. 809–815.
- L. Smith, T. Ibn-Mohammed, S. C. L. Koh, and I. M. Reaney, *Appl. Energy* **220**, 496 (2018).
- S.-H. Yoon, M.-Y. Kim, and D. Kim, *J. Mater. Chem. C* **8**(27), 9373 (2020).
- P. Ren, Z. Liu, Q. Wang, B. Peng, S. Ke, H. Fan, and G. Zhao, *Sci. Rep.* **7**(1), 6693 (2017).
- S. Ke and H. Huang, *J. Appl. Phys.* **108**(6), 064104 (2010).
- J. Liu, F. Li, Y. Zeng, Z. Jiang, L. Liu, D. Wang, Z. G. Ye, and C. L. Jia, *Phys. Rev. B* **96**(5), 054115 (2017).
- A. E. Glazounov, A. K. Tagantsev, and A. J. Bell, *Phys. Rev. B* **53**(17), 11281 (1996).
- T. Li, X. Lou, X. Ke, S. Cheng, S. Mi, X. Wang, J. Shi, X. Liu, G. Dong, H. Fan, Y. Wang, and X. Tan, *Acta Mater.* **128**, 337 (2017).
- S. Horiuchi and S. Ishibashi, *Chem. Sci.* **12**(42), 14198 (2021).
- F. Yan, H. Bai, G. Ge, J. Lin, C. Shi, K. Zhu, B. Shen, J. Zhai, and S. Zhang, *Small* **18**(10), 2106515 (2022).
- Z. Lu, G. Wang, W. Bao, J. Li, L. Li, A. Mostaed, H. Yang, H. Ji, D. Li, A. Feteira, F. Xu, D. C. Sinclair, D. Wang, S.-Y. Liu, and I. M. Reaney, *Energy Environ. Sci.* **13**(9), 2938 (2020).
- X. Wang, Y. Fan, Z. Bin, A. Mostaed, L. Li, A. Feteira, D. Wang, D. C. Sinclair, G. Wang, and I. M. Reaney, *J. Eur. Ceram. Soc.* **42**(15), 7381 (2022).
- H. Ji, D. Wang, W. Bao, Z. Lu, G. Wang, H. Yang, A. Mostaed, L. Li, A. Feteira, S. Sun, F. Xu, D. Li, C.-J. Ma, S.-Y. Liu, and I. M. Reaney, *Energy Storage Mater.* **38**, 113 (2021).
- H. Qi, R. Zuo, A. Xie, A. Tian, J. Fu, Y. Zhang, and S. Zhang, *Adv. Funct. Mater.* **29**(35), 1903877 (2019).
- X. Hao, J. Zhai, L. B. Kong, and Z. Xu, *Prog. Mater. Sci.* **63**, 1–57 (2014).
- L. Li, P. Fan, M. Wang, N. Takesue, D. Salamon, A. N. Vtyurin, Y. Zhang, H. Tan, B. Nan, Y. Lu, L. Liu, and H. Zhang, *J. Phys. D* **54**(29), 293001 (2021).
- G. Wang, Z. Lu, Y. Li, L. Li, H. Ji, A. Feteira, D. Zhou, D. Wang, S. Zhang, and I. M. Reaney, *Chem. Rev.* **121**(10), 6124 (2021).
- Z. Liu, T. Lu, J. Ye, G. Wang, X. Dong, R. Withers, and Y. Liu, *Adv. Mater. Technol.* **3**(9), 1800111 (2018).
- H. Pan, S. Lan, S. Xu, Q. Zhang, H. Yao, Y. Liu, F. Meng, E.-J. Guo, L. Gu, D. Yi, X. Renshaw Wang, H. Huang, J. L. MacManus-Driscoll, L.-Q. Chen, K.-J. Jin, C.-W. Nan, and Y.-H. Lin, *Science* **374**(6563), 100 (2021).
- H. Yang, Z. Lu, L. Li, W. Bao, H. Ji, J. Li, A. Feteira, F. Xu, Y. Zhang, H. Sun, Z. Huang, W. Lou, K. Song, S. Sun, G. Wang, D. Wang, and I. M. Reaney, *ACS Appl. Mater. Interfaces* **12**(39), 43942 (2020).
- T. Correia, M. Stewart, A. Ellmore, and K. Albertsen, *Adv. Eng. Mater.* **19**(6), 1700019 (2017).
- Z. Dai, D. Li, Z. Zhou, S. Zhou, W. Liu, J. Liu, X. Wang, and X. Ren, *Chem. Eng. J.* **427**, 131959 (2022).
- N. Zhao, H. Fan, L. Ning, J. Ma, and Y. Zhou, *J. Am. Ceram. Soc.* **101**(12), 5578 (2018).
- Z. Lu, W. Bao, G. Wang, S.-K. Sun, L. Li, J. Li, H. Yang, H. Ji, A. Feteira, D. Li, F. Xu, A. K. Kleppe, D. Wang, S.-Y. Liu, and I. M. Reaney, *Nano Energy* **79**, 105423 (2021).
- Y. Fan, W. Wang, and J. Zhao, *Ceram. Int.* **46**(8), 12269 (2020).
- A. Xie, H. Qi, and R. Zuo, *ACS Appl. Mater. Interfaces* **12**(17), 19467 (2020).
- T. Li, H. Fan, C. Long, G. Dong, and S. Sun, *J. Alloys Compd.* **609**, 60 (2014).
- T. Li, C. Liu, P. Shi, X. Liu, R. Kang, C. Long, M. Wu, S. Cheng, S. Mi, Y. Xia, L. Li, D. Wang, and X. Lou, *Adv. Funct. Mater.* **32**(32), 2202307 (2022).
- T. Gnanasekaran, R. K. Dayal, and B. Raj, *Nuclear Corrosion Science and Engineering*, edited by D. Féron (Woodhead Publishing, 2012), p. 301.
- M. Hasegawa, *Treatise on Process Metallurgy* (Elsevier, 2014), p. 507.
- L. Yang, X. Kong, F. Li, H. Hao, Z. Cheng, H. Liu, J.-F. Li, and S. Zhang, *Prog. Mater. Sci.* **102**, 72 (2019).
- R. Zuo, H. Qi, J. Fu, J. Li, M. Shi, and Y. Xu, *Appl. Phys. Lett.* **108**(23), 232904 (2016).
- H. Qi, R. Zuo, J.-F. Li, and L. Li, *J. Eur. Ceram. Soc.* **38**(16), 5341 (2018).
- H. Abdelkefi, H. Khemakhem, G. Vélú, J. C. Carru, and R. Von der Mühl, *Solid State Sci.* **6**(12), 1347 (2004).
- S. H. Cha and Y. H. Han, *Jpn. J. Appl. Phys., Part 1* **45**(10R), 7797 (2006).
- H. Kishi, N. Kohzu, J. Sugino, H. Ohsato, Y. Iguchi, and T. Okuda, *J. Eur. Ceram. Soc.* **19**(6–7), 1043 (1999).
- J. Pokorný, U. M. Pasha, L. Ben, O. P. Thakur, D. C. Sinclair, and I. M. Reaney, *J. Appl. Phys.* **109**(11), 114110 (2011).
- Y. I. Yuzyuk, *Phys. Solid State* **54**(5), 1026 (2012).
- C. Long, Q. Chang, Y. Wu, W. He, Y. Li, and H. Fan, *J. Mater. Chem. C* **3**(34), 8852 (2015).
- Y. Shimakawa, Y. Kubo, Y. Nakagawa, T. Kamiyama, H. Asano, and F. Izumi, *Appl. Phys. Lett.* **74**(13), 1904 (1999).
- S.-H. Yoon, J.-H. Lee, D.-Y. Kim, and N. M. Hwang, *J. Am. Ceram. Soc.* **86**, 88–92 (2002).
- A. J. Chiquito, C. A. Amorim, O. M. Berengue, L. S. Araujo, E. P. Bernardo, and E. R. Leite, *J. Phys.: Condens. Matter* **24**(22), 225303 (2012).